Inorganic Chemistry

pubs.acs.org/IC

Article

Hourglass-Shaped Homo- and Heteronuclear Nonanuclear Lanthanide Clusters: Structures, Magnetism, Photoluminescence, and Theoretical Analysis

Priya Pandey, Deepanshu Chauhan, Mrinalini G. Walawalkar, Sandeep K. Gupta, Franc Meyer, Gopalan Rajaraman,* and Ramaswamy Murugavel*

Cite This: *Inorg. Chem.* 2024, 63, 11963−11976

Read Online

ACCESS | Metrics & More | Article Recommendations | Supporting Information

ABSTRACT: Synthesis of nonameric cationic clusters $[Dy_9(acac)_{16}(\mu_3\text{-}OH)_8(\mu_4\text{-}OH)_2]OH{\cdot}6H_2O$ (**1**), $[Dy_8Tb(acac)_{16}(\mu_3\text{-}OH)_8(\mu_4\text{-}OH)_2]OH{\cdot}2H_2O$ (**2**), and $[Gd_9(acac)_{16}(\mu_3\text{-}OH)_8(\mu_4\text{-}OH)_2]OH{\cdot}6H_2O$ (**3**) (acac = acetylacetonate) is reported. The emission spectrum of **1** shows Dy(III) ion characteristic bands assignable to the $^4F_{9/2} \rightarrow {}^6H_J$ (J = 15/2 to 9/2) transitions. Emission due to both Dy(III) and Tb(III) ions is observed for **2** in the visible range, with Tb(III) specific bands appearing due to the $^5D_4 \rightarrow {}^7F_J$ (J = 6, 4, and 3) transitions. Cluster **3** exhibits a significant magnetocaloric effect (MCE), with $-\Delta S_m$ values increasing with decrease in temperature and increase in field, reaching $-\Delta S_m^{max}$ = 20.98 J kg^{-1} K^{-1} at 2 K and 9 T. Isotropic magnetic coupling constants (J_s) in **3** derived from density functional theory (DFT) calculations reveal that the exchange interactions are antiferromagnetic and weak. Compound **3** possesses S = 7/2 ground state arising from the central Gd(III) ion along with several nested excited states due to competing antiferromagnetic interactions that yield reasonably large MCE values. Utilizing computed exchange coupling interactions, we have performed ab initio CASSCF/RASSI-SO/POL_ANISO calculations on antiferromagnetic **1** and **2** to estimate the exchange interactions using the Lines model. For **2**, Dy(III)···Tb(III) exchange interactions were extracted for the first time and were found to be weakly antiferromagnetically coupled.

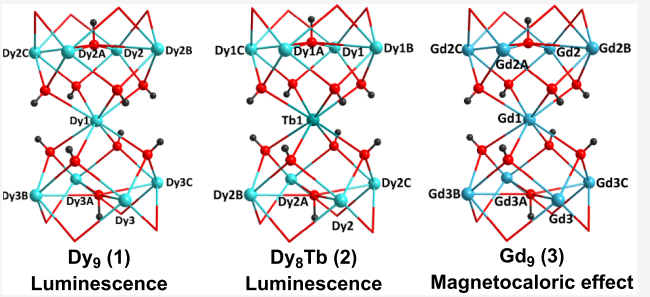

INTRODUCTION

Lanthanide (Ln) molecular complexes have gained significant interest across a wide range of disciplines, which include catalysis,[1] magnetic resonance imaging,[2] luminescent materials,[3] multimodal imaging probes,[4] single-molecule magnets (SMMs),[5−7] and quantum information processing (QIP).[8] Over the last few decades, numerous Ln-based clusters have been reported, with nuclearities such as Ln_3,[9] Ln_4,[10,11] Ln_5,[12−17] Ln_6,[18] Ln_8,[9] Ln_9,[9,16,17] Ln_{10},[19] Ln_{12},[20] Ln_{16},[21] Ln_{19},[22] Ln_{36},[23] Ln_{48},[24,25] Ln_{104},[26] etc. An interesting aspect of these clusters is their luminescence properties with characteristic emission wavelengths spanning across visible to near-infrared regions.[27−29] Among the Ln(III) ions, Tb and Eu are well known for their exceptional photoluminescence (PL) behavior, which can be attributed to an intramolecular energy transfer from the electronic states associated with the organic complex to localized intra-4f shell energy levels of the ions.[30−32] Being highly shielded, 4f electrons present in Ln ions exhibit magnetic and spectroscopic properties of the free parent ion (ligand field effects are marginal). Thus, their orbital momentum is almost unquenched, and they have a well-defined distribution of electronic levels, resulting in sharp and easily identifiable 4f−4f electronic transitions.[32−34]

Apart from their impressive luminescence properties, Ln(III) complexes have been gaining significant attention in the emerging area of molecular spin qubits and quantum gates (QGs). These complexes are being explored for their potential to manipulate spins and perform quantum logic operations. Logic QGs such as controlled-NOT (C-NOT) and SWAP gates manage quantum computation operations.[35,36] Achieving universal quantum gates involves arranging two weakly coupled and asymmetric lanthanide ions, particularly in the case of C-NOT gates. Aromí and co-workers in 2014 introduced heterobimetallic lanthanide complexes as promising candidates for processing quantum information in quantum computers.[35,37] The preparation of heteronuclear coordination systems, which involve different types of metal ions, is acknowledged as challenging yet interesting, as quantum gates.

Received: January 25, 2024
Revised: May 16, 2024
Accepted: June 4, 2024
Published: June 13, 2024

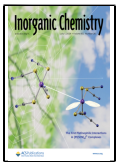

Scheme 1. Synthetic Protocol for the Preparation of the Complexes 1−3

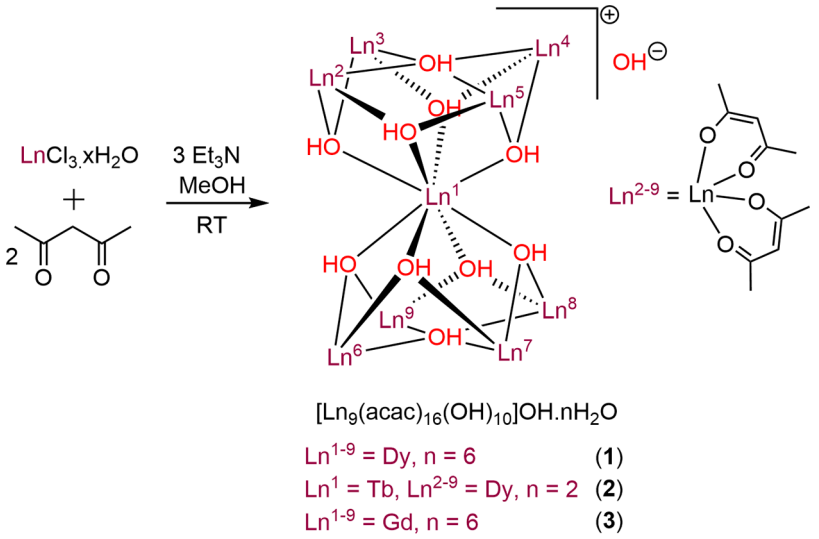

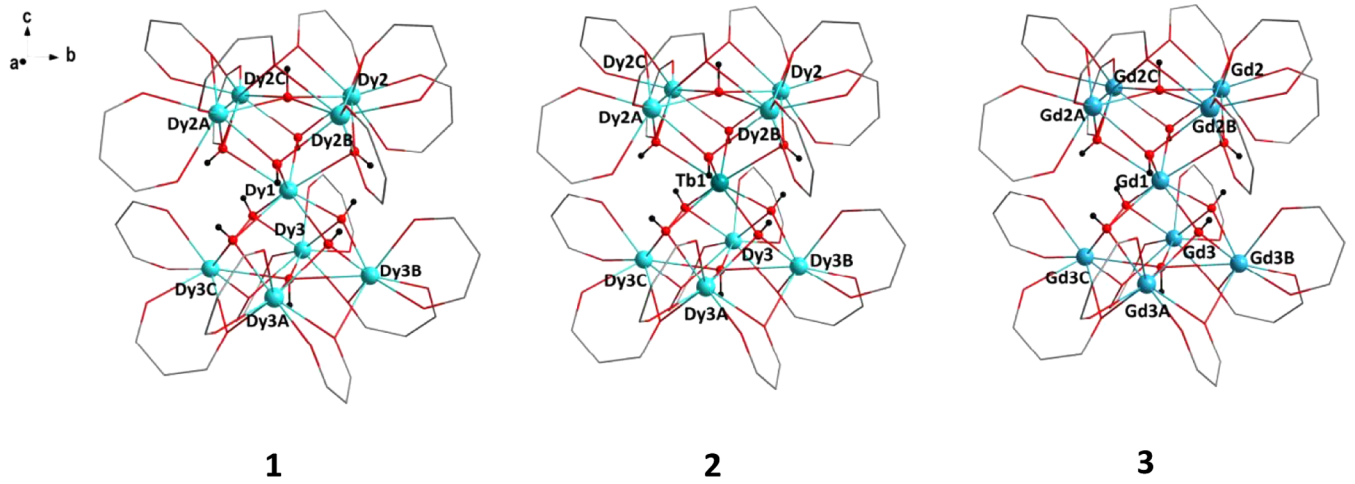

Figure 1. Molecular structure of compounds **1**−**3** (methyl groups of acac ligands, lattice OH ion, and lattice water molecules are omitted for clarity; symmetry codes: A = 1.5 − x, 1.5 − y, z; B = 1.5 − x, y, z; and C = x, 1.5 − y, z).

Besides, Ln(III)-based clusters have also been reported to exhibit significant magnetocaloric effect and hence act as molecular refrigerants and can potentially render conventional refrigeration techniques obsolete.[38,39] To be a promising magnetic coolant, a compound should possess negligible magnetic anisotropy, a large spin ground state (S), quenched orbital momentum (D = 0), weak superexchange interaction, and high magnetic density.[40,41] Among the Ln(III) ions, Gd(III) based clusters, possessing almost all of the above requirements, have been investigated widely, establishing themselves as potential candidates to display appreciable MCE.[42−44]

Synthesis of Ln(III)-based clusters with a desired nuclearity in a controlled manner is a challenging task.[45−49] The choice of pH, solvent, temperature, reaction time, and ligand: metal-ion ratio plays an important role in modulating the composition and architecture of the isolated Ln(III) clusters. Among the cluster types, Ln_9 nonanuclear lanthanide clusters having an "hourglass"-like core have been studied in some detail (Table S1).[32,50−57] Given the wide utility of such polynuclear clusters described above, we have investigated in the present study a new series of nonanuclear isostructural Ln cationic clusters $[Dy_9(acac)_{16}(\mu_3\text{-}OH)_8(\mu_4\text{-}OH)_2]OH{\cdot}6H_2O$ (**1**), $[Dy_8Tb(acac)_{16}(\mu_3\text{-}OH)_8(\mu_4\text{-}OH)_2]OH{\cdot}2H_2O$ (**2**), and $[Gd_9(acac)_{16}(\mu_3\text{-}OH)_8(\mu_4\text{-}OH)_2]OH{\cdot}6H_2O$ (**3**), where the Ln(III) ions are bridged by hydroxyl groups and acac ligands, thereby facilitating strong interaction between the Ln(III) ions within the cluster. Compounds **1** and **2** made up of Dy(III) and Tb(III) ions have been studied for their photoluminescence behavior, while the Gd cluster **3** has been investigated for its magnetocaloric behavior.

RESULTS AND DISCUSSION

Synthesis and Characterization of Complexes 1−3. Nonameric lanthanide hydroxide clusters, $[Dy_9(acac)_{16}(\mu_3\text{-}OH)_8(\mu_4\text{-}OH)_2]OH{\cdot}6H_2O$ (**1**), $[Dy_8Tb(acac)_{16}(\mu_3\text{-}OH)_8(\mu_4\text{-}OH)_2]OH{\cdot}2H_2O$ (**2**), and $[Gd_9(acac)_{16}(\mu_3\text{-}OH)_8(\mu_4\text{-}OH)_2]OH{\cdot}6H_2O$ (**3**) (acac = acetylacetonate) (Scheme 1) have been prepared from the reaction of correct stoichiometric amounts of respective hydrated Ln(III) chloride salt(s) with acetylacetone in the presence of triethylamine and methanol under mild conditions (Scheme 1). These clusters are soluble in dimethyl sulfoxide (DMSO) and dichloromethane and not in water, methanol, and acetonitrile in spite of their ionic

https://doi.org/10.1021/acs.inorgchem.4c00332
Inorg. Chem. 2024, 63, 11963−11976

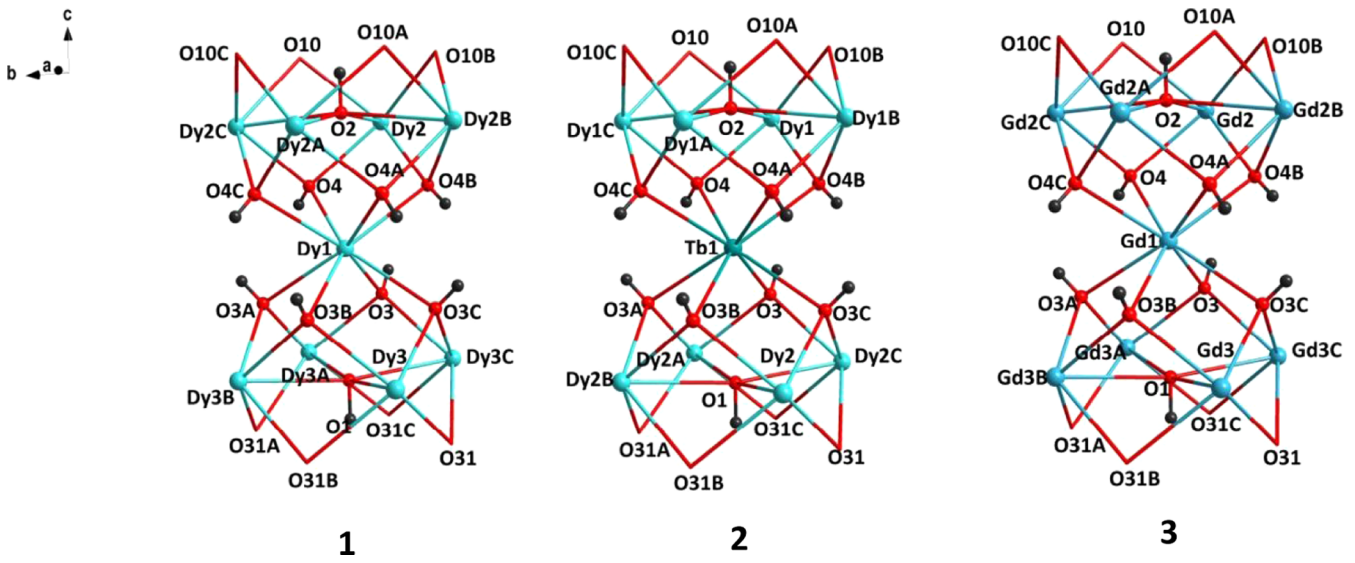

Figure 2. Core structure of **1**−**3** (acac ligands present on the Ln(III) ion, lattice OH ion, and lattice water molecules are omitted for clarity; symmetry codes: *A* = 1.5 − *x*, 1.5 − *y*, *z*; *B* = 1.5 −*x*, *y*, *z*; and C = *x*, 1.5−*y*, *z*).

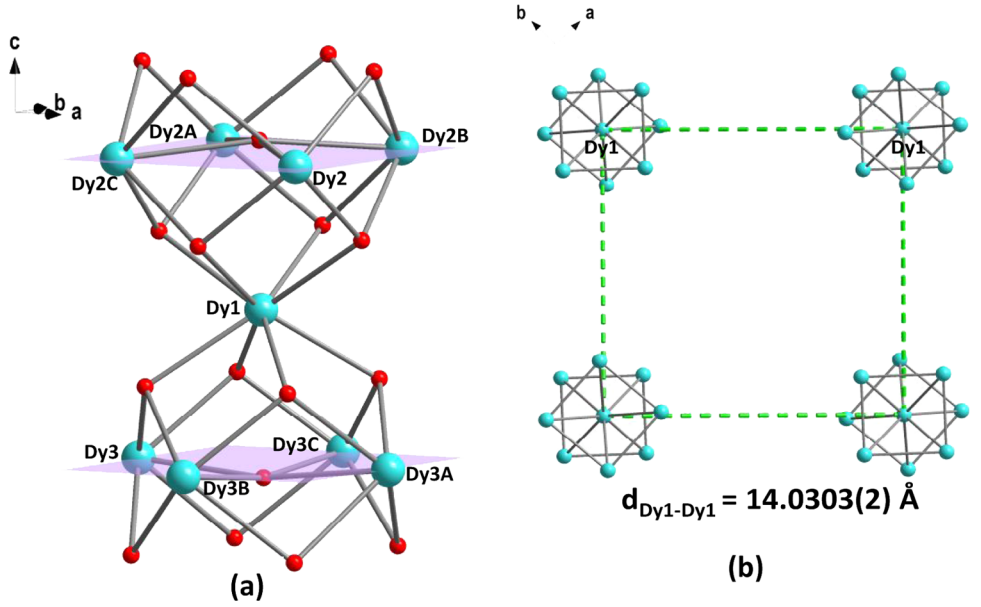

Figure 3. (a) Representation of the basal plane connecting four Dy(III) centers at the top and four Dy(III) centers at the bottom in compound **1**. (b) Crystal packing arrangement of **1** along the *c*-axis with internuclear Dy1−Dy1 bond distance; dashed green line shows the internuclear bond distance between two Dy atoms (acac ligands present on the Ln(III) ion, lattice OH ion, and lattice water molecules are omitted for clarity). Color scheme: cyan, Dy; red, O.

character. The nonaclusters are one of the many products formed in these reactions in very low yields that have been carefully separated from the rest of the product. Compounds **1**−**3** have been characterized by spectroscopic and analytical methods, and molecular structures have been identified by single-crystal X-ray diffraction analysis.

Compounds **1**−**3** yield almost identical Fourier transform infrared (FT-IR) spectra (Figures S1−S3). The broad band appearing in the range 3500−3200 cm^{-1} corresponds to the −OH stretching frequency of μ_4-OH and μ_3-OH bonds. The weak absorption bands in the range 3000−2900 cm^{-1} is assigned to unsaturated as well as saturated C−H stretching frequency of the acetylacetone ligand. The band appearing around 1600−1500 cm^{-1} reveals the presence of conjugated carbonyl and C═C functional groups. The characteristic absorption band for the M−O stretching vibration is present in the range 890−750 cm^{-1} for all compounds. Compounds **1**−**3** exhibited stable thermal behavior up to 200 °C, as shown by thermogravimetric analysis (TGA) (Figure S4).

Single-Crystal X-ray Diffraction Studies. Single-crystal X-ray diffraction data reveal that clusters **1**−**3** are isostructural and crystallize in the tetragonal *P*4/*n* space group. Selected bond lengths and bond angles of **1**−**3** are presented in Tables S2−S7.

Hence, only the structure of cluster **1** is described here in detail as a representative case. Clusters **1**−**3** contain a 4-fold axis passing through the central Dy1 atom as shown in Figure 1. The cationic part of the nonameric cluster **1** contains 9 metal ions distributed in 3 layers in a 4:1:4 configuration, 16 acac ligands, 8 μ_3-OH anions, and 2 μ_4-OH groups.[56] One OH

https://doi.org/10.1021/acs.inorgchem.4c00332
Inorg. Chem. 2024, 63, 11963−11976

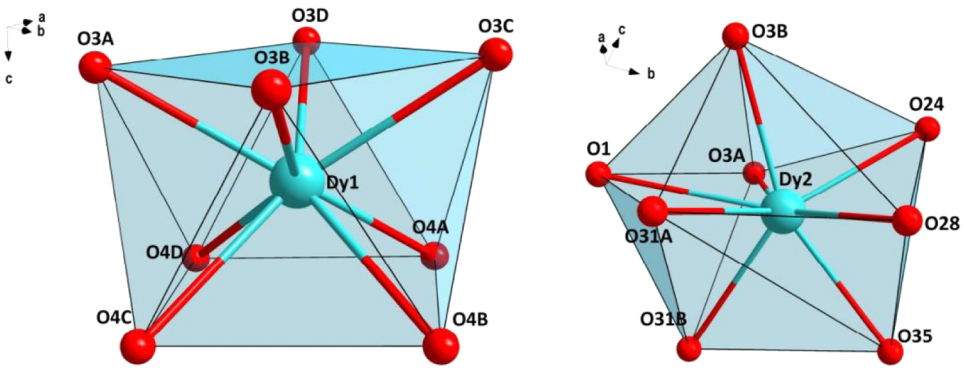

Figure 4. Polyhedral view around the different coordinated Dy(III) centers of **1**; the geometry around the central Dy1 is square antiprism and for the peripheral Dy2 biaugmented trigonal prism configuration. Metal polyhedra in **2** and **3** are identical to compound **1**.

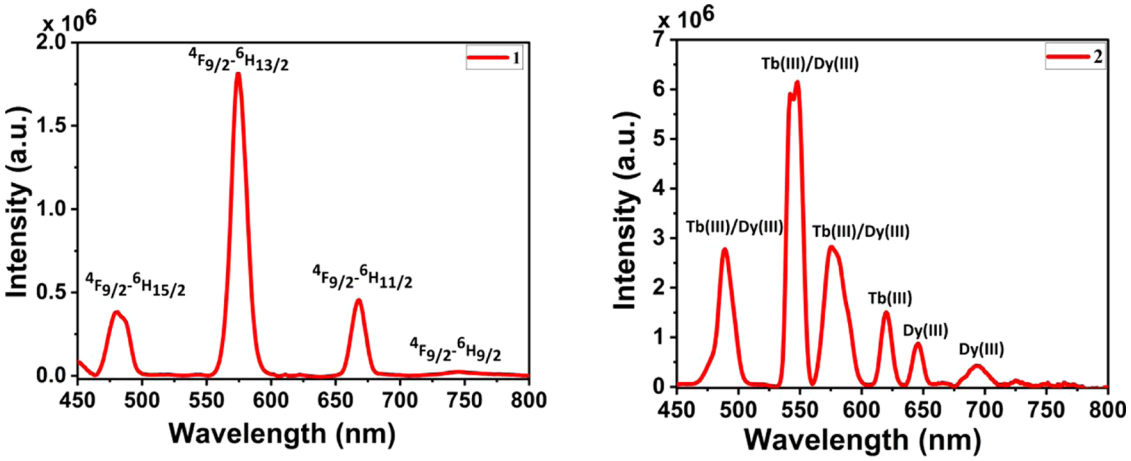

Figure 5. Emission spectra of **1** (left) and **2** (right) in DMSO at room temperature (λ_{ex} = 320 nm).

anion outside the coordination sphere maintains the electroneutrality in the structure. Additionally, there are six lattice water molecules present in homometallic species **1** and **3**, whereas heterometallic **2** contains only two water molecules in the lattice. Thus, the upper and lower rims of **1** are made up of $Ln_4(\mu_4\text{-OH})$ units (rim 1 = Dy2, Dy2A, Dy2B, Dy2C; rim 2 = Dy3, Dy3A, Dy3B, Dy3C), which sandwich the ninth lanthanide ion at the center of the cluster (Figures 2, 3 and S5). In other words, cluster **1** contains two basal planes having four Dy atoms, each forming pentanuclear square pyramid that share the apical Dy1 center. The Dy atoms present on the triangular faces of these pyramids are capped by μ_3-OH groups with the Dy1···Dy2 and Dy1···Dy3 distances being 3.7130(4) and 3.7038(4) Å, respectively (Figure 3a). Further, the basal plane Dy atoms are capped by μ_4-OH groups with Dy2···Dy2B (or Dy2C) and Dy2···Dy2A distances of 3.5826(5) and 5.0666(5) Å, respectively. Similar distances at the other basal plane or rim are Dy3···Dy3B (or Dy3C) = 3.6152(5) Å and Dy3···Dy3A = 5.1127(5) Å (Figure 3a). The distance between the planes is 5.8200(1) Å. Each μ_4-OH group is shifted by about 0.24 Å above the basal Dy_4 plane, slightly lower than the reported in the literature for other Ln_9 clusters.[58] The rim Dy(III) centers are surrounded by 16 acetylacetonate ligands that are divided into 2 groups, 8 of which chelate a given lanthanide ion while the other 8 chelate a metal ion and also bridge an adjacent metal ion through one of the oxygen centers (Figure S6).

The overall molecular structure of **1**−**3** possesses a well-known "diabolo" or "hourglass" shape as shown in Figure 2. The intermolecular Dy···Dy distance between the adjacent central Dy atoms is 14.0303(2) Å, as seen from the packing diagram in Figure 3b. Furthermore, the clusters have two distinct coordination environments around Dy ions. The central Dy1 is connected to the eight peripheral Dy(III) center through eight μ_3-OH anion, whereas the basal Dy atoms are interconnected through μ_4-OH in the nearly regular parallelogram. The presence of hydroxyl groups in the cluster promotes intramolecular hydrogen bonding, thereby increasing the stability of the structure (Table S8).

The exact determination of the shape around nonequivalent Dy(III) centers (Dy1 and Dy2) is carried out by SHAPE 2.1 software.[59] Central Dy1 atom shows a square antiprism coordination geometry, while peripheral Dy atoms, i.e., Dy2/Dy3 display biaugmented trigonal prism coordination geometry with *CShMs* (the Continuous Shape Measures values) of 0.36 (D_{4d}) and 1.537 (C_{2v}) for Dy1 and Dy2 (or Dy3), respectively (Tables S9 and S10). The coordination polyhedron views of Dy1 and Dy2 (or Dy3) atoms are shown in Figure 4.

The relatively lower yields of Ln_9 clusters limit the bulk synthesis of compounds **1**−**3**. Therefore, powder X-ray diffraction analysis measurements for bulk purity had to be carried out using samples collected from different batches (Figure S7). Nevertheless, the powder X-ray diffraction patterns of the bulk material collected from different batches correlate well with the simulated pattern derived from single-crystal X-ray diffraction patterns, indicating the purity of the compound.

https://doi.org/10.1021/acs.inorgchem.4c00332
Inorg. Chem. 2024, 63, 11963−11976

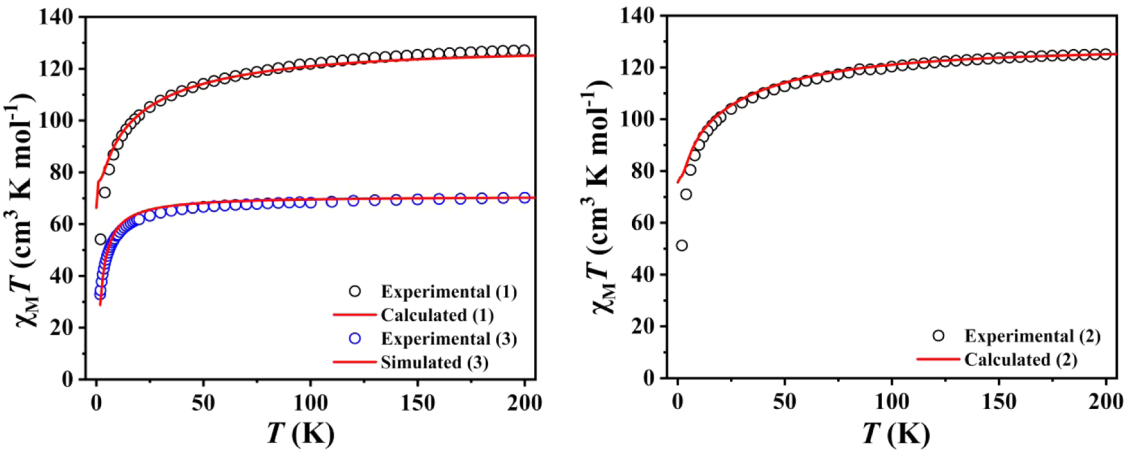

Figure 6. Temperature dependence of $\chi_M T$ for **1**−**3** clusters at 0.5 T. The simulation of the susceptibility was performed using computed J values from DFT and POLY_ANISO simulations. As there are simulations from independent calculations, error on the J values can not be estimated.

Luminescence Spectra Studies. The UV−vis absorption spectra of **1**−**3** were recorded in solution (DMSO, conc. = 1×10^{-3} M) as well as solid state in the range of 200−800 nm at room temperature. In solution, the excitation spectra (Figures S8 and S9) show broad features in the region 260−320 nm for compounds **1**−**3**. These features can be assigned to $\pi-\pi^*$ and $n-\pi^*$ transitions of the acetylacetonate ligand. The solid-state excitation of complexes **1** and **2** shows ligand as well as respective Dy(III) and Tb(III) ion-based peaks within the range 325−500 nm, whereas **3** shows only ligand-based peaks centered at 290 nm (Figure S10).

The luminescence properties of **1**−**3** in solution (DMSO) and the solid state were investigated at room temperature. Excitation of complex **1** in DMSO at 320 nm shows characteristic sharp emission bands for Dy(III) ion in the range 481−752 nm that can be assigned to $^4F_{9/2} \rightarrow {}^6H_{15/2}$ (481 nm), $^4F_{9/2} \rightarrow {}^6H_{13/2}$ (575 nm), $^4F_{9/2} \rightarrow {}^6H_{11/2}$ (664 nm), and $^4F_{9/2} \rightarrow {}^6H_{9/2}$ (753 nm) electronic transitions (Figure 5, left).[32,60,61] Similarly, for mixed lanthanide cluster **2**, both Dy(III) and Tb(III) ions are known to emit in the same visible spectral region. The emission spectrum of **2** exhibits peaks from both Dy(III) (λ_{em} = 480, 576, 646, and 698 nm) and Tb(III) (λ_{em} = 488, 548, and 620 nm) for this mixed metal cluster (Figure 5, right). Well-resolved luminescence bands in the visible region appearing at 488, 548, and 620 nm indicate transitions from $^5D_4$ excited states of the Tb(III) ion to the ^7F_J (J = 6−3) lower energy states, respectively. Hence, the emission spectra of **1** and **2** show characteristic luminescence of Dy(III) and Tb(III) ions upon excitation at 320 nm, which is the absorption band of acetylacetonate ligand.[62] This can be explained by the energy transfer mechanism in the lanthanide complexes proposed by Dexter. Based on Dexter's theory,[63] the suitability of the energy difference between the resonance level of the Ln(III) ion and the triplet state of the ligand is a key factor affecting the energy transitions of the lanthanide complexes.

In cluster **3**, upon excitation at 300 nm, the spectrum showed a broad emission band in the range 400−450 nm originating from acetylacetonate ligand. This can be attributed to the fact that the Gd(III) ion lacks luminescent features (Figure S9). Similar solid-state emission patterns were observed for complexes **1**−**3** (Figure S11), and they are comparable to the solution PL spectra but for some minor changes (Figure S11). The observed differences are due to the fact that the emission properties of a complex can vary significantly due to differences in molecular packing and interactions in the two different states. In the solid state, molecules are often closely packed, leading to increased intermolecular interactions that can affect the emission properties.[64] In contrast, in solution, molecules are more mobile and experience weaker intermolecular interactions, leading to emission properties that are typically closer to those of isolated molecules. Therefore, solvation effects can influence the emission properties in solution.[65] The emission wavelength in the solid state is red-shifted compared with that in the solution state for all three complexes.

As can be seen from Figure 5, compounds **1** and **2** show luminescence behavior in the visible range, whereas the Gd(III) analog **3** does not. The quantum yield calculations for complexes **1**−**3** showed values of 11 and 13% for **1** and **2**, respectively, and 6.6% for **3**.

Magnetic Studies. Variable-temperature magnetic susceptibility measurements for complexes **1**−**3** were carried out on the polycrystalline samples under an applied direct current (dc) field of 0.5 T in the temperature range of 2−200 K (Figure 6).[7,66] At 200 K, the $\chi_M T$ (χ_M = molar magnetic susceptibility) values are 127.13, 125.08, and 70.99 cm^3 K mol^{-1} for complexes **1**, **2**, and **3**, respectively. These are in good agreement with the expected theoretical values of 127.64 cm^3 K mol^{-1} for nine isolated Dy(III) ions ($^6H_{15/2}$, S = 5/2, L = 5, g = 4/3) in complex **1**, 125.35 cm^3 K mol^{-1} for eight isolated Dy(III) and one noninteracting Tb(III) ions ($^7F_6$, S = 3, L = 3, g = 3/2) in complex **2**, and 70.92 cm^3 K mol^{-1} for nine Gd(III) ions ($^8S_{7/2}$, S = 7/2, L = 0, g = 2) in complex **3**. The $\chi_M T$ value gradually decreases upon cooling for complexes **1** and **2** until 50 K, before sharply falling to 54.12 cm^3 K mol^{-1} for **1** and 56.24 cm^3 K mol^{-1} for **2** at 2 K. The $\chi_M T$ value remains almost constant for the Gd(III) complex **3** upon cooling and sharply decreases below 20 K reaching a value of 34.40 cm^3 K mol^{-1} at 2 K. The decrease in the magnetic susceptibility values from 127.13 to 54.12 cm^3 K mol^{-1} for **1**, 125.08 to 56.24 cm^3 K mol^{-1} for **2**, and 70.99 to 34.40 cm^3 K mol^{-1} for **3** can be due to the intermolecular magnetic exchange/depopulation of the Stark sublevels. Curie−Weiss analysis of the magnetic susceptibility data yields θ = −5.19 K for **1**, −5.44 K for **2**, and −3.04 K for **3** indicating overall antiferromagnetic interactions (Figure S12).

https://doi.org/10.1021/acs.inorgchem.4c00332
Inorg. Chem. 2024, 63, 11963−11976

Field-dependent magnetization measurements were performed for complexes **1**−**3** in the magnetic field range of 0−7 T in the temperature range of 2.0−10.0 K for **1** and **2** (Figures S13 and S14) and in the temperature range of 2.0−20.0 K for **3** between 0 and 9 T (Figure 7). The magnetization

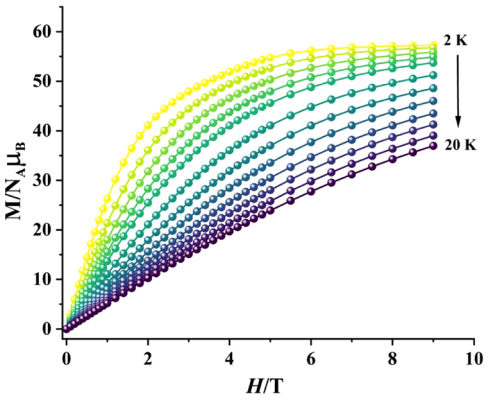

Figure 7. Plot of M versus H of compound **3** in the temperature range of 2−20 K.

(M) at 2 K for **1** and **2** increases linearly at lower magnetic fields and then gradually reaches 55.35 μ_B for **1** and 56.91 μ_B for **2** at 7 T without saturation, much lower than the expected M_{sat} values of 90 μ_B for **1** and 89 μ_B for **2**, respectively, indicating significant magnetic anisotropy. In the case of complex **3**, the magnetization increases sharply and linearly at lower magnetic fields at 2 K, subsequently reaching 57.68 μ_B with saturation at 9 T, which is almost close to the expected value of 63 μ_B for **3**.

Alternate current (ac) susceptibility measurements were also performed for complexes **1** and **2**, both in the absence and presence of the applied dc field. However, no out-of-phase component of ac susceptibility (χ_M'') was observed signifying the absence of slow relaxation of magnetization in these clusters within the operating range of temperature of our SQUID magnetometer (Figures S15−S18).

In the context of advancing molecular magnetic refrigerant materials, polynuclear gadolinium-based clusters are known in the literature for showing a significant magnetocaloric effect.[67,68] The magnetic entropy changes for compound **3** were calculated from the magnetization data (Figure 7) according to the Maxwell equation: $\Delta S_m(T)_{\Delta H} = \int[\partial M\, \partial T]_H dH$. The plot of $-\Delta S_m$ versus T (Figure 8) clearly demonstrates the magnetic entropy change ($-\Delta S_m$) of **3** gradually increases with a decrease in temperature (20−2 K) as well as the increase in the field (0−9 T). The experimental $-\Delta S_m^{max}$ for **3** is 20.98 J kg^{-1} K^{-1} at T = 2.0 K with 9.0 T is lower than the theoretically calculated value of 47.21 J kg^{-1} K^{-1} for nine uncorrelated Gd(III) ions (S = 7/2) deduced from the equation—$\Delta S_m = nR\ln(2S + 1)$ (where n is the number of gadolinium atoms, R is the gas constant, and S is the spin state).[45] The significant dissimilarity in the experimental and calculated entropy changes is attributed to the antiferromagnetic interactions between the gadolinium metal ions. Table S11 shows a comparative literature of $-\Delta S_m$ values for various polynuclear Gd$_n$ ($n \geq 4$) clusters. These results show that nonameric cluster **3** shows a significant magnetocaloric effect and can be used as a magnetic refrigerant coolant.

Theoretical Studies. To understand the magnetic properties of the nonanuclear cluster, we have performed DFT[69] and

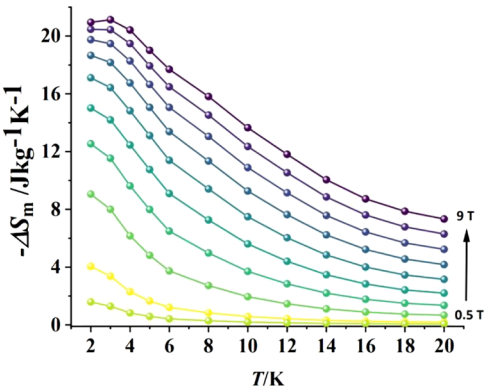

Figure 8. Plot of change in magnetic entropy ($-\Delta S_m$) versus T for **3** at 0−9.0 T from 2 to 20 K.

ab initio CASSCF/RASSI-SO/SINGLE_ANISO[70,71] calculations (see Computational Details in the Experimental Section for more information).

Evaluation of Isotropic Magnetic Exchange in Complex 3. To begin with, broken symmetry (BS) DFT calculations were performed on complex **3** to estimate the isotropic magnetic exchange coupling constant among the Gd(III) ions. A careful look at the geometry reveals three different exchange interactions in complex **3** (see Figures 9,

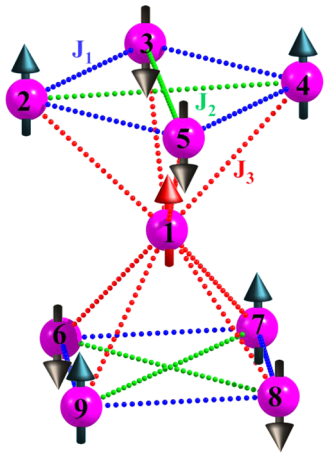

Figure 9. Magnetic exchange pathways (J_1−J_3) for complex **3**. Upward- and downward-facing arrows indicate spin-up and spin-down configurations, respectively.

S19, and S20). The J_1 interaction describes the coupling between two Gd(III) ion centers bridged by acac ligand bridge (∠Gd−O−Gd 96.9°) angle and one μ_3-OH bridge (∠Gd−O−Gd 103.2°). The J_2 interaction is the diagonal interaction in the {Gd4} moiety mediated via a μ_4-OH bridge (∠Gd−O−Gd = 169.2°). The J_3 interaction between the {Gd4} square the central Gd(III) ion mediated via two μ_3-OH bridges (∠Gd−O−Gd of 102.7 and 104.1°). This is necessary considering the earlier magneto-structural correlation proposed by Rajaraman and co-workers.[72] The DFT calculated J_1−J_3 are −0.056, −0.022, and −0.052 cm^{-1}, respectively. Earlier magneto-structural correlation predicts that the Gd−Gd exchange is expected to be ferromagnetic only when the Gd−O−Gd angle lies in the range of 105−135° and here all of the angles are found to lie outside this range and, therefore, expected to be antiferromagnetic as computed from DFT calculations.[72,73]

https://doi.org/10.1021/acs.inorgchem.4c00332
Inorg. Chem. 2024, 63, 11963−11976

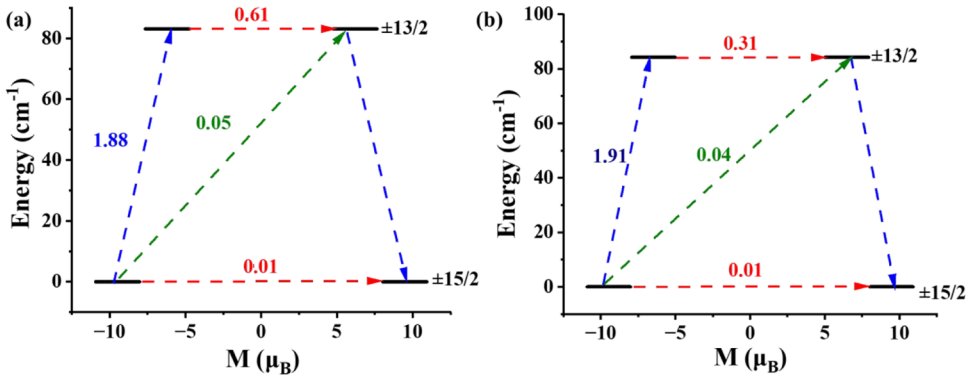

Figure 10. Single-ion magnetization relaxation dynamics of the (a) Dy9 center in complex **1** and (b) Dy8 center in complex **2**.

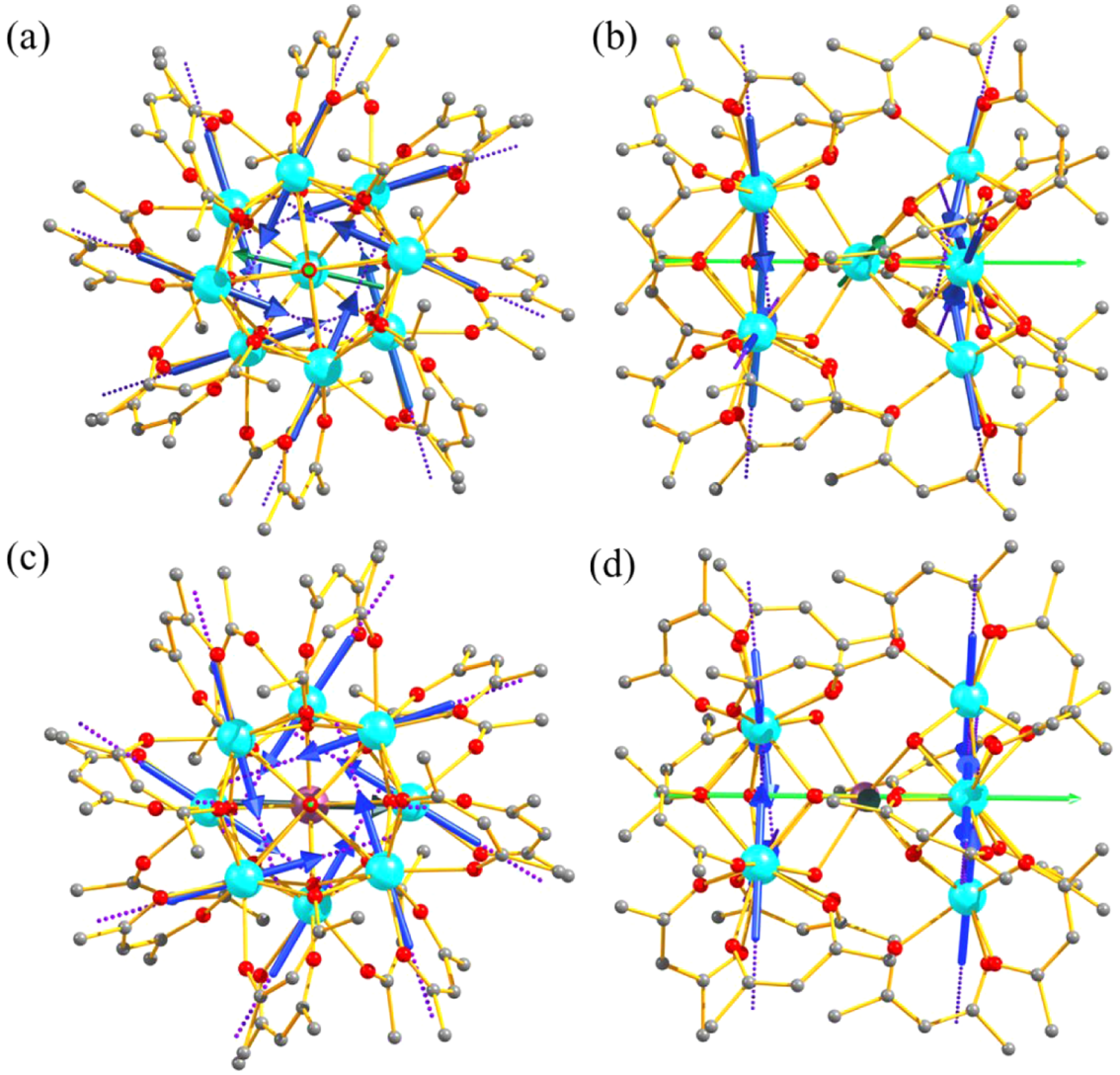

Figure 11. Orientation of magnetic anisotropic axes in complexes **1** and **2**. (a) Top view and (b) side view of **1**. (c) Top view and (d) side view of **2**. Hydrogen atoms are omitted for clarity. Color scheme: Dy, cyan; Tb, light brown; O, red; C, gray. The dark blue arrow shows the direction of the ground state anisotropy axis for the Dy(III) ion, the dotted violet line indicates the extension of the ground state anisotropic axes in both directions, the dark green arrow shows the ground state anisotropy axis direction for the Tb(III) ion, and the light green line in (b) and (d) represents the pseudo-S_8 axis direction.

The earlier observed parabolic behavior suggests that a lower angle would yield strong antiferromagnetic Gd···Gd interactions, which is observed here with $J_1 > J_3 \gg J_2$. This is essentially due to weak ferromagnetic contribution J_s that arise due to charge-transfer interaction to the 5d/6s orbital and weak but non-negligible 4f−4f orbital overlap that tends to get larger both in acute and wider angles, as illustrated earlier.[72,74] As the simulation of susceptibility for this cluster is not

https://doi.org/10.1021/acs.inorgchem.4c00332
Inorg. Chem. 2024, 63, 11963−11976

possible using the exact diagonalization method, we have adopted a fragment approach and have considered the {Gd5} fragment interacting with a {Gd4} fragment employing DFT J_s. This is found to reproduce the experimental susceptibility, offering confidence in the methodology chosen. This is expected to result in an $S = 7/2$ ground state located at the central Gd(III) ion, as shown in Figure S20. The J_1 and J_2 interactions, although both are antiferromagnetic, are competing interactions with J_1 being dominant. Due to these competing interactions, the excited states of higher multiplicity are expected to be lower in energy and closer to the $S = 7/2$ state. This leads to the observation of relatively large MCE, which is unexpected given that the exchange interactions are antiferromagnetic. Our analysis reveals that within 1 cm^{-1} of the energy window, several states of higher multiplicity were found, and such nesting of states rationalizes the magnetization curve observed at 2 K. Such competing exchange coupling as a strategy to obtain larger MCE has been suggested earlier.[73]

Mechanism of Magnetization Relaxation in Complexes 1 and 2. *Magnetic Relaxation Mechanism due to Single-Ion Behavior.* Initially, we performed the single-ion calculation on complexes **1** and **2** by substituting the Ln(III) ions with the La(III) ion as a diamagnetic ion to understand the magnetic properties. All nine Kramers Dy(III) ions in complex **1** showed the ground-first excited state gap of 51.3, 44.3, 49.4, 58.9, 23.8, 63.0, 79.9, 79.4, and 83.1 cm^{-1}, respectively (see Figure S21 and Table S12). The ground state computed *g*-anisotropies with all nine centers exhibiting Ising anisotropy g_{zz} = 18.674, 18.560, 18.661, 18.785, 18.686, 18.890, 18.895, and 18.951 for Dy1−9 in complex **1**. In complex **2**, the computed ground-first excited state gap for eight Dy(III) ions are 58.0, 54.2, 52.9, 73.3, 79.4, 84.2, 91.6, and 81.0 cm^{-1}, respectively (see Figure S19 and Table S14), and the corresponding Ising *g*-anisotropic g_{zz} values are 18.823, 18.707, 18.713, 18.920, 18.760, 18.925, 18.966, and 18.811. A significant transverse anisotropy was found for all of the Dy(III) single-ion models, suggesting strong ground state tunneling and no SMM behavior (Figure 10). This is witnessed in the magnetization relaxation mechanism constructed by using ab initio calculations (see Figures 11 and S22). Although the exchange coupling is expected to quench the tunneling, the *J* values are weak and unlikely to quench the quantum tunneling of magnetization (QTM) observed. This is also supported by the computed crystal-field (CF) parameters that indicate the presence of a large nonaxial component (in which $q \neq 0$ and $k = 2, 4, 6$) than an axial component (in which $q = 0$ and $k = 2, 4, 6$), supporting prominent QTM effects (see Tables S13 and S19). The g_{zz} axis of the {Dy4} square units was found to align along the terminal oxygen atom of the ligand and, therefore, devoid of any expected torodicity.[75,76] To understand the anisotropic axis direction, we carried out the LoProp charge analysis (see Figure S23). The g_{zz} axis is directed along the terminal oxygen atom of the ligand and pointed between the bridging oxygen atom, minimizing the electrostatic repulsion, as expected for an oblate ion.

The central Dy(III) ion possessing a pseudo-D_{4d} geometry was found to have significant transverse anisotropy with a close-lying excited state. The g_{zz} axis for this Dy(III) ion pointed along the pseudo-C_2 axis similar to those found in [DyO8] complexes possessing square antiprism geometry (see Table S17).[77] The geometry is found to deviate from perfect D_{4d} symmetry (with a twist angle of 43.4°) that is found to enable QTM from the ground state (see Figure 12). In

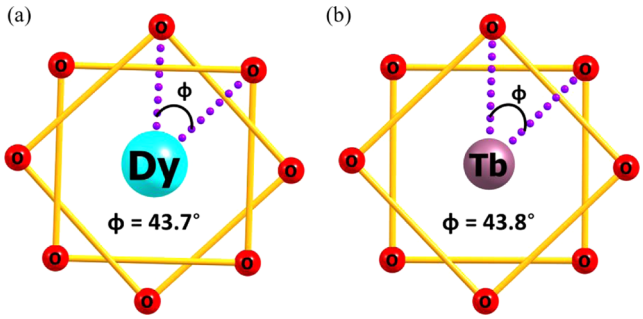

Figure 12. Comparison of the twist angle (a) for central Dy in **1** and (b) for central Tb in **2**.

complex **2**, on the other hand, Tb(III) ion was found to have $m_J = \pm 6$ ground state; however, with the observed twist angle, the tunnel splitting is expected to be more significant, as seen in the computed results (see Table S15).[6] Further, the first excited state was also close-lying (11 cm^{-1}), suggesting faster relaxation for the Tb(III) ion.

The β-electron density of the central Dy(III) and Tb(III) ion is plotted in Figure S24 and suggests the oblate nature of the density but lacks pure oblicity, suggesting a mixture of m_J states as observed in the ab initio calculations.

The single-ion magnetization relaxation in pseudo-D_{4d} complexes depends on the twist angle (ϕ). This larger deviation leads to a significant perturbation in the two orthogonal ground state sublevels of Dy(III)/Tb(III) ion, which results in the QTM. Hence, there is no SMM observed.

Relaxation Mechanism of the Cluster. To understand the mechanism of magnetization relaxation of the full complex, we have simulated the susceptibility data using the Lines model, employing the POLY_ANISO program. Here, the following exchange Hamiltonian was used.

$$\hat{H}_{ex} = -\sum_{i=1}^{3} \tilde{J}_{iz} \times \tilde{S}_{iz} \times \tilde{S}_{i+1z}$$

where $\tilde{S}_{iz}$ represents pseudospin projection on the anisotropy axis of the *i*th center and illustrates two states with reversed maximal magnetization on the magnetic site.

The Lines model[70] computed exchange coupling for complexes **1** and **2** are given in Table 1. Here, J_1 and J_2 interactions in both complexes **1** and **2** describe exchange coupling among the Dy(III) ions possessing Ising anisotropy at the ground $m_J = \pm 15/2$ ground state. These interactions are estimated to be antiferromagnetic, with J_2 being weaker than J_1, which is similar to that of complex **3**. However, the estimated coupling is significantly stronger due to a large contribution from the dipolar interactions. As complexes **1** and **2** are isostructural, it is anticipated that J_1−J_3 is revealed by the POLY_ANISO simulation. The J_3 interaction in complex **1** describes Dy(III)···Dy(III) ion coupling, while in complex **2**, it describes Dy(III)···Tb(III) ion coupling. Both of these interactions are found to be antiferromagnetic, while the latter interaction is slightly weaker than the former. This is the first time the Dy(III)···Tb(III) ion interactions are estimated in the literature, and it is found to be (i) antiferromagnetic despite the difference in percent of oblate electron density of $m_J = \pm 15/2$ and ± 6 for Dy(III) and Tb(III) ions, respectively, and (ii) the strength of the interaction is relatively weaker and this is attributed to the variation in the orientation of g_{zz} as it is

https://doi.org/10.1021/acs.inorgchem.4c00332
Inorg. Chem. 2024, 63, 11963−11976

Table 1. Computed POLY_ANISO and DFT Estimated Magnetic Exchange Interactions in Complexes 1 and 2 (All Values Are Given in cm^{-1})

	J_1			J_2			J_3			
complex	J_{exch}	J_{dip}	J_{tot}	J_{exch}	J_{dip}	J_{tot}	J_{exch}	J_{dip}	J_{tot}	zJ
1	−0.056	−0.565	−0.621	−0.022	−0.28	−0.302	−0.052	−0.469	−0.521	−0.005
2	−0.056	−0.565	−0.621	−0.022	−0.28	−0.302	−0.063	−0.388	−0.451	−0.005

tilted by 74.04 and 94.52° for Dy(III) and Tb(III) ions with respect to the pseudo-S_8 axis, respectively.

The POLY_ANISO simulation reveals very strong QTM at the bunch of ground state KD's generated in complex **1**, suggesting that weak coupling is present between Dy(III)···Dy(III) ion, which is insufficient to quench the QTM observed at the single-ion level. Hence, out-of-phase signals are not expected even in an applied field, as evidenced in the experiments. For complex **2**, on the other hand, the ground state is non-Kramers in nature and was found to have significant tunnel splitting of 0.28 cm^{-1} between 2 sets of 64 pseudo-doublets. Such a strong tunnel splitting suggests very strong tunneling that can be quenched by the application of a field, as observed in the experiments.

However, such tunneling, which ensured a vigorous mixing of wave function among the pseudo-doublet states, is an essential criterion for quantum bits, particularly in developing multi-Qbit C-NOT gates. Complex **2**, possessing 132 pseudo-doublets with a significant tunnel splitting, suggests strong coherence among states, the manipulation of which can help in the design of multi-Qbit molecular systems. As Tb(III) ion nuclear spin has been accurately read out using single-crystal micro-SQUID measurements in recent times,[78] complex **2** offers a unique opportunity to look at the influence of the ground state $m_J = \pm 6$ that is coupled with other Dy8 pseudo-doublets.

CONCLUSIONS

Hourglass-shaped air- and moisture-stable Ln_9 clusters Dy_9, Gd_9, and Dy_8Tb_1 reported in the present study exhibit multifunctional properties. These complexes have been characterized by spectroscopy and X-ray crystallography. Notably, complexes **1** and **2** demonstrate pronounced photoluminescence in the visible range compared to the Gd(III) analogue **3**. Complex **3**, on the other hand, displays a significant magnetocaloric effect, with the entropy change ($-\Delta S_m$) reaching 20.98 J kg^{-1} K^{-1} at 2.0 K in the applied field of 9.0 T. Furthermore, detailed DFT calculations were employed to extract isotropic magnetic coupling parameters in complex **3**, revealing weak antiferromagnetic interactions. Ab initio CASSCF/RASSI-SO calculations on complexes **1** and **2** allowed estimation of their exchange interactions, indicating antiferromagnetic coupling as well. The heteronuclear complex **2**, which facilitated the estimation of Dy(III)···Tb(III) exchange interactions for the first time, presents prospects for advancing multi-Qbit C-NOT gates. The strong quantum tunnel splitting observed in complex **2**, with the presence of Tb(III) ion nuclear spin, leads to a unique feature for potential quantum information processing applications.

EXPERIMENTAL SECTION

Materials and Physical Property Studies. All reactions were carried out under ambient conditions without any precautions to exclude air or moisture. Starting materials such as acetylacetone (Hacac) (Sigma-Aldrich), triethylamine, $DyCl_3{\cdot}xH_2O$, and $TbCl_3{\cdot}xH_2O$, and $GdCl_3{\cdot}xH_2O$ (Alfa Aesar) were procured from commercial sources and used without any further purification. All of the starting materials and the products were found to be stable toward moisture and air. The melting points were measured in glass capillaries and reported as uncorrected. Elemental analyses were performed on a Vario MICRO cube microanalyzer. Fourier transform infrared spectra were recorded on a PerkinElmer Spectrum One Infrared Spectrometer as KBr diluted disks within the 4000−400 cm^{-1} frequency range. The thermal behavior (Rigaku, Thermo Plus EVO2) was evaluated under a nitrogen atmosphere at a heating rate of 10 °C min^{-1}. UV−visible spectra were obtained on a Shimadzu UV-NIR-3600 double-beam spectrophotometer with a bandpass of 2.0 nm. Spectroscopic grade dimethyl sulfoxide (DMSO) solvent was used from Spectrochem UV spectroscopy. Baseline correction was done in the same solvent used for sample dissolution. Fluorescence spectra were recorded on a Horiba Fluoromax 4 spectrofluorometer having a Xe flash lamp as the excitation source and with an emission bandpass of 5 nm using a 1 cm path length quartz cuvette. Absorbance and emission of complexes **1**−**3** were recorded in dimethyl sulfoxide solvent (Spectrochem UV spectroscopy) with a concentration of the stock solution of 10^{-3} M and diluted further for measurements. Luminescence quantum yields were measured according to conventional procedures,[79] with diluted solutions using Quinine sulfate in 0.1 M H_2SO_4 (Φf = 0.55) as reference. All measurements were conducted at room temperature. Powder X-ray diffraction data were obtained at room temperature on a Rigaku SmartLab SE diffractometer by using Cu Kα radiation (λ = 1.54190 Å). Inductively coupled plasma atomic emission spectroscopy (ICP-AES) analysis was performed using a SPECTRO Analytical Instruments GmbH, Germany, ARCOS, Simultaneous ICP Spectrometer instrument proceeded digestion in acid and are quoted as weight percentages.

Preparation of $[Dy_9(acac)_{16}(\mu_3\text{-}OH)_8(\mu_4\text{-}OH)_2]OH{\cdot}6H_2O$ *(**1**).* A mixture of acetylacetone (Hacac, 1.0 mmol) and triethylamine (1.5 mmol) was added dropwise to a methanolic solution of $DyCl_3{\cdot}xH_2O$ (0.5 mmol, 188 mg). After 15 min of stirring, the clear colorless mixture was filtered, and the filtrate was left undisturbed at room temperature. Yellow block-shaped single crystals as minor product along with colorless needles (major product) were formed after 5 days, suitable for X-ray diffraction analysis. These crystals were separated under an optical microscope. The yellow block-shaped crystals were found to be of the title compound **1**, while the major product, which is colorless needles of $Dy(acac)_3{\cdot}2H_2O$, has been reported in the literature.[80] Yield (%): 128 mg (34% based on metal salt); M_p: >200 °C; FT-IR (KBr diluted, cm^{-1}) ν_{max}: 3399 (OH, br), 3146 ($C_{sp}{}^2$-H, s), 2983 ($C_{sp}{}^3$-H, w), 1615 (C═O, s), 1514 (vs), 1396 (vs), 1256 (w), 1019 (w), 923 (w), 776 (w); Anal. Calc. (%) for $C_{80}H_{135}Dy_9O_{49}$ (FW = 3343.37) found (calc.): C, 28.74 (29.08); H, 3.51 (3.90).

https://doi.org/10.1021/acs.inorgchem.4c00332
Inorg. Chem. 2024, 63, 11963−11976

Table 2. Crystal Data and Structure Refinements for Clusters 1−3

compound	1	2	3
identification code	RM_PP_4_14	RM_PP_4_141	RM_PP_6_35
empirical formula	$C_{80}H_{135}Dy_9O_{49}$	$C_{80}H_{127}Dy_8O_{45}Tb$	$C_{80}H_{135}Gd_9O_{49}$
formula weight	3343.37	3267.73	3296.12
temperature/K	108(4)	150(1)	108(4)
crystal system	tetragonal	tetragonal	tetragonal
space group	$P4/n$	$P4/n$	$P4/n$
a/Å	18.8778(2)	19.0744(4)	18.8786(2)
c/Å	15.3219(2)	15.4794(6)	15.3811(3)
volume/Å^3	5460.3(1)	5631.9(3)	5481.9(2)
Z	2	2	2
ρ_{calc}/g cm^{-3}	2.034	1.927	1.990
μ/mm^{-1}	6.161	5.933	5.447
$F(000)$	3202.0	3120.0	3144.0
crystal size/mm^3	0.04 × 0.08 × 0.15	0.02 × 0.065 × 0.07	0.022 × 0.107 × 0.109
radiation/Å	Mo Kα (λ = 0.71073)	Mo Kα (λ = 0.71073)	Mo Kα (λ = 0.71073)
2Θ range/deg	3.424−49.996	4.006−49.986	4.04−49.978
reflections	76,669	75,912	70,420
Ind. Refl.	4821	4958	4834
data/restr./param.	4821/0/334	4958/4/338	4834/0/328
GooF on F^2	1.032	1.150	1.049
final R indexes [$I \geq 2\sigma(I)$]	R_1 = 0.0180	R_1 = 0.0277	R_1 = 0.0215
	wR_2 = 0.0400	wR_2 = 0.0589	wR_2 = 0.0511
final R indexes [all data]	R_1 = 0.0216	R_1 = 0.0316	R_1 = 0.0267
	wR_2 = 0.0416	wR_2 = 0.0619	wR_2 = 0.0532
largest diff. peak/hole/e Å^{-3}	1.73/−0.80	1.04/−0.80	1.03/−0.88

Preparation of $[Dy_8Tb(acac)_{16}(\mu_3\text{-}OH)_8(\mu_4\text{-}OH)_2]OH{\cdot}2H_2O$ (2). The synthetic procedure was the same as that in the case of **1**, only the mole ratio of metal precursors was varied. $DyCl_3{\cdot}xH_2O$ (0.445 mmol, 168 mg) and $TbCl_3{\cdot}xH_2O$ (0.055 mmol, 21 mg) were used in the synthesis to yield the title compound **2**. Yield (%): 50 mg (14% based on metal salt); M_p: >200 °C; FT-IR (KBr diluted, cm^{-1}) ν_{max}: 3221 (OH, br), 2977 (C_{sp^2}-H, w), 2921 (C_{sp^3}-H, w), 1614 (C═O, m), 1467 (m), 1265 (w), 1184 (s), 1067 (s), 890 (s), 769 (w), 688 (w); ICP-AES: calcd. Dy: 89%; Tb: 11%; found: Dy: 88.5%; Tb: 11.5%; Anal. Calc. (%) for $C_{80}H_{127}Dy_8O_{45}Tb$ (FW = 3267.73); found (calc.): C, 29.51 (28.77); H, 4.64 (4.07).

Preparation of $[Gd_9(acac)_{16}(\mu_3\text{-}OH)_8(\mu_4\text{-}OH)_2]OH{\cdot}6H_2O$ (3). A similar synthesis procedure to **1** was employed. $GdCl_3{\cdot}xH_2O$ (0.5 mmol, 183 mg) was taken instead of $DyCl_3{\cdot}xH_2O$ and was reacted with 2 equiv of Hacac. Yield (%): 18 mg (5% based on metal salt); M_p: >200 °C; FT-IR (KBr diluted, cm^{-1}) ν_{max}: 3381 (OH, br), 3002 (C_{sp^2}-H, w), 2895 (C_{sp^3}-H, w), 1533 (C═O, s), 1493 (s), 1426 (m), 1381 (s), 1255 (w), 1022 (w), 910 (w), 854 (w), 758 (w); Anal. Calc. (%) for $C_{80}H_{135}Gd_9O_{49}$ (FW = 3296.12); found (calc.): C, 29.65 (29.15); H, 3.59 (4.13).

Crystallographic Data Collection and Refinement. Single crystals of **1**−**3** were obtained directly from the reaction mixture by slow evaporation of the solvent at room temperature. A suitable crystal of each compound was mounted on a Bruker D8 QUEST single-crystal diffractometer using a Mo Kα radiation source (λ = 0.71073 Å) for unit cell determination and diffraction intensity data collection. Data integration and indexing were carried out using the CrysAlisPro software suite.[81] Using Olex2,[82] the structure was solved with the ShelXT[83] structure solution program using intrinsic phasing and refined with the ShelXL[84] refinement package using least-squares minimization. All nonhydrogen atoms were refined anisotropically. The hydrogen atoms were refined isotropically as rigid atoms in their idealized locations. All figures were drawn using Diamond 3.2 software.[85] CCDC 2326855−2326857 for **1**−**3** clusters contain the supplementary crystallographic data for this article, which can be obtained free of charge from the Cambridge Crystallographic Data Centre. The data collection and refinement processes are summarized in Table 2.

Magnetic Measurements. Magnetic measurements for complexes **1** and **2** were carried out with a Quantum-Design MPMS3 SQUID magnetometer. The powdered samples were packed in a polycarbonate capsule and covered with low-viscosity perfluoropolyether-based inert oil Fomblin Y45 in a nonmagnetic sample holder. Magnetic measurements for complex **3** were carried out with a Quantum-Design PPMS DynaCool magnetometer. The powdered samples were packed in a nonmagnetic sample holder. Each raw data for the measured magnetic moment was corrected for the diamagnetic contribution of the capsules including the inert oil if used according to $M_{dia}(\text{capsule}) = \chi_g \times m \times H$, with an experimentally obtained gram susceptibility of the capsules including the inert oil. The molar magnetic susceptibility data were corrected for the diamagnetic contribution. For complexes **1** and **2**, 15.5 and 16.0 mg of powdered sample were packed in a polycarbonate capsule weighing 31.1 and 31.6 mg and covered with 23.14 and 24.2 mg of inert oil Fomblin Y45, respectively. For complex **3**, 5.74 mg of powdered sample was packed in a polypropylene powder holder weighing 186.86 mg. Experimental data were modeled with the julX_2s program.[86] Alternating current (ac) susceptibility measurements were carried out for compounds **1** and **2** in an oscillating ac field of 3 Oe and frequencies ranging from 100 to 800 Hz.

Computational Details. Using the MOLCAS 8.2 program,[87] ab initio CASSCF/RASSI-SO/SINGLE_ANISO

https://doi.org/10.1021/acs.inorgchem.4c00332
Inorg. Chem. 2024, 63, 11963−11976

calculations were carried out on the single-crystal XRD structure without any further geometry optimization. Owing to the high atom count, a model for complexes **1** and **2** has been constructed using the atomic locations found through X-ray diffraction (Figure S25). A diamagnetic La(III) ion has been used to replace the other metal ions in calculating the magnetic characteristics of a single paramagnetic Ln(III) ion. It has been suggested that the Douglas−Kroll Hamiltonian[88] illustrates the relativistic effect of Ln(III) ions. The basis set used in this work is from the ANO-RCC library. In particular, the basis sets [ANO-RCC···8s7p5d3f2g1h] and [ANO-RCC···7s6p4d2f] have been used for paramagnetic Dy(III) ion, [ANO-RCC···3s2p] for O atoms, [ANO-RCC···3s2p] for N atoms, [ANO-RCC···3s2p] for the C atom, and [H.ANO-RCC···2s] for H atoms to perform the GUESSORB calculations to determine the active space for the complete active space self-consistent field (CASSCF) calculations.[89] For Dy(III) ions, we have utilized CAS (9,7), and for Tb(III) ions, CAS (8,7). The sextet (21 roots) of Dy(III) ions, as well as the septet (7 roots), quintet (140 roots), and triplets (195 roots) of Tb(III) ions, were calculated using the state-averaged CASSCF method. Spin−orbit coupling was used in RASSI-SO to mix roots for the Dy(III) ion, 21 sextets, 7 septets, 140 quartets, and 112 triplets. Furthermore, the SINGLE_ANISO software[70] has considered these calculated spin−orbital (SO) states to determine the *g*-tensor and crystal-field (CF) parameters. To obtain a better understanding of the magnetic relaxation mechanism, the CF parameters were examined. The corresponding crystal-field Hamiltonian is given in the equation:

$$\hat{H}_{CF} = \sum \sum_{k=-q}^{q} B_k^q \tilde{O}_k^q$$

where B_k^q is the crystal-field parameter and $\tilde{O}_k^q$ is Steven's operator.

Dipole−dipole magnetic couplings between the Ln(III) centers and magnetic properties of the complexes, including the four Ln(III) metal centers, were obtained using the POLY_ANISO routine.[71]

Using the Gaussian 09 suite of software, the density functional theory (DFT) with the B3LYP functional was used to calculate the magnetic exchange interactions. The magnetic exchange *J* value has been computed using the DFT calculations in conjunction with the broken symmetry (BS) technique.[69] J_1, J_2, and J_3 parametrize the magnetic exchange interaction between Ln2−Ln3, Ln2−Ln4, and Ln1−Ln4. The spin-only Gd(III) ions were substituted for the Ln(III) ions, and their spin was then rescaled to that of the Dy(III)/Tb(III) ions. Here, the Cundari−Stevens (CS) relativistic effective core potential on the Gd(III) atom[90] has been employed using a double-ξ quality basis set, while the triple-ξ valence basis set has been used for the remaining atoms. By entering the ab initio data into a model intramolecular magnetic coupling Hamiltonian, the real energy spectrum, wave function, and magnetic texture calculations, as well as the modeling of the magnetic observations were performed.

■ ASSOCIATED CONTENT

Supporting Information

The Supporting Information is available free of charge at https://pubs.acs.org/doi/10.1021/acs.inorgchem.4c00332.

Spectral characterization data, tables of X-ray crystallographic analysis, dc and ac magnetic data, additional figures and tables for computational studies (PDF)

Accession Codes

CCDC 2326855−2326857 contain the supplementary crystallographic data for this paper. These data can be obtained free of charge via www.ccdc.cam.ac.uk/data_request/cif, by emailing data_request@ccdc.cam.ac.uk, or by contacting The Cambridge Crystallographic Data Centre, 12 Union Road, Cambridge CB2 1EZ, UK; fax: +44 1223 336033.

■ AUTHOR INFORMATION

Corresponding Authors

Ramaswamy Murugavel − *Department of Chemistry, Indian Institute of Technology Bombay, Mumbai 400076, India;* orcid.org/0000-0002-1816-3225; Email: rmv@chem.iitb.ac.in

Gopalan Rajaraman − *Department of Chemistry, Indian Institute of Technology Bombay, Mumbai 400076, India;* orcid.org/0000-0001-6133-3026; Email: rajaraman@chem.iitb.ac.in

Authors

Priya Pandey − *Department of Chemistry, Indian Institute of Technology Bombay, Mumbai 400076, India*

Deepanshu Chauhan − *Department of Chemistry, Indian Institute of Technology Bombay, Mumbai 400076, India*

Mrinalini G. Walawalkar − *Department of Chemistry, Indian Institute of Technology Bombay, Mumbai 400076, India*

Sandeep K. Gupta − *Institute of Inorganic Chemistry, University of Göttingen, Göttingen D-37077, Germany; Department of Chemistry, Indian Institute of Technology Delhi, New Delhi 110016, India;* orcid.org/0000-0003-2432-933X

Franc Meyer − *Institute of Inorganic Chemistry, University of Göttingen, Göttingen D-37077, Germany;* orcid.org/0000-0002-8613-7862

Complete contact information is available at: https://pubs.acs.org/10.1021/acs.inorgchem.4c00332

Notes

The authors declare no competing financial interest.

■ ACKNOWLEDGMENTS

R.M. acknowledges SERB, New Delhi, for funding this work through SPR/2019/001145, CRG/2022/002406, and SB/S2/JCB-85/2014. G.R. acknowledges CRG/2022/001697 and SB/SJF/2019-20/12 for funding. P.P. acknowledges IIT Bombay for a research fellowship, and D.C. is thankful to UGC for SRF fellowship. The authors thank SAIF, IIT Bombay, and RIFC-funded central facilities (IOE funding) for access to various instruments. S.K.G. thanks the Alexander von Humboldt Foundation and the International Centre of the University of Göttingen for postdoctoral research fellowships. S.K.G. also thanks IIT Delhi for the support and facilities. The purchase of the SQUID magnetometer was supported by the DFG (project number 423442764 INST 186/1329-1FUGG) and the Niedersächsische Ministerium für Wissenschaft und Kultur (MWK).

DEDICATION

Dedicated to Professor Vinod Singh on the occasion of his 65th birthday.

REFERENCES

(1) Rossi, L. M.; Costa, N. J. S.; Silva, F. P.; Wojcieszak, R. Magnetic nanomaterials in catalysis: advanced catalysts for magnetic separation and beyond. *Green Chem.* **2014**, *16*, 2906−2933.

(2) Bottrill, M.; Kwok, L.; Long, N. J. Lanthanides in magnetic resonance imaging. *Chem. Soc. Rev.* **2006**, *35*, 557−571, DOI: 10.1039/b516376p.

(3) Costa, I. F.; Blois, L.; Paolini, T. B.; Assunção, I. P.; Teotonio, E. E. S.; Felinto, M. C. F. C.; Moura, R. T., Jr; Longo, R. L.; Faustino, W. M.; Carlos, L. D.; Malta, O. L.; Carneiro Neto, A. N.; Brito, H. F. Luminescence properties of lanthanide tetrakis complexes as molecular light emitters. *Coord. Chem. Rev.* **2024**, *502*, No. 215590, DOI: 10.1016/j.ccr.2023.215590.

(4) Liu, N. A.-O.; Homann, C. A.-O.; Morfin, S.; Kesanakurti, M. S.; Calvert, N. D.; Shuhendler, A. A.-O.; Al, T.; Hemmer, E. A.-O. Core-multi-shell design: unlocking multimodal capabilities in lanthanide-based nanoparticles as upconverting, T_2-weighted MRI and CT probes. *Nanoscale* **2023**, *15*, 19546−19556.

(5) Gupta, S. K.; Murugavel, R. Enriching lanthanide single-ion magnetism through symmetry and axiality. *Chem. Commun.* **2018**, *54*, 3685−3696.

(6) Atkin, A. M.; Giansiracusa, M. J.; Calvello, S.; Rousset, E.; Gable, R. W.; Phonsri, W.; Murray, K. S.; Howard, J. K.; Soncini, A.; Mole, R. A.; Boskovic, C. Inelastic Neutron Scattering Measurement of the Ground State Tunneling Gap in Tb and Ho Analogues of a Dy Field-Induced Single-Molecule Magnet. *Inorg. Chem.* **2023**, *62*, 1141−1155.

(7) Borah, A.; Murugavel, R. Magnetic relaxation in single-ion magnets formed by less-studied lanthanide ions Ce(III), Nd(III), Gd(III), Ho(III), Tm(II/III) and Yb(III). *Coord. Chem. Rev.* **2022**, *453*, No. 214288, DOI: 10.1016/j.ccr.2021.214288.

(8) Aguilà, D.; Roubeau, O.; Aromí, G. Designed polynuclear lanthanide complexes for quantum information processing. *Dalton Trans.* **2021**, *50*, 12045−12057.

(9) Langley, S. K.; Moubaraki, B.; Murray, K. S. Trinuclear, octanuclear and decanuclear dysprosium(III) complexes: Synthesis, structural and magnetic studies. *Polyhedron* **2013**, *64*, 255−261.

(10) Yan, P.-F.; Lin, P.-H.; Habib, F.; Aharen, T.; Murugesu, M.; Deng, Z.-P.; Li, G.-M.; Sun, W.-B. Planar Tetranuclear Dy(III) Single-Molecule Magnet and Its Sm(III), Gd(III), and Tb(III) Analogues Encapsulated by Salen-Type and β-Diketonate Ligands. *Inorg. Chem.* **2011**, *50*, 7059−7065.

(11) Wu, Y.; Morton, S.; Kong, X.; Nichol, G. S.; Zheng, Z. Hydrolytic synthesis and structural characterization of lanthanide-acetylacetonato/hydroxo cluster complexes - A systematic study. *Dalton Trans.* **2011**, *40*, 1041−1046.

(12) Peng, J.-B.; Kong, X.-J.; Ren, Y.-P.; Long, L.-S.; Huang, R.-B.; Zheng, L.-S. Trigonal Bipyramidal Dy_5 Cluster Exhibiting Slow Magnetic Relaxation. *Inorg. Chem.* **2012**, *51*, 2186−2190.

(13) Andrews, P. C.; Hennerdorf, F.; Junk, P. C.; Thielemann, D. T. Variable Nuclearity in Lanthanoid Coordination Chemistry. *Eur. J. Inorg. Chem.* **2014**, *2014*, 2849−2854.

(14) Andrews, P. C.; Deacon, G. B.; Gee, W. J.; Junk, P. C.; Urbatsch, A. Synthesis and Characterisation of Thiophene-Functionalised Lanthanoid Diketonate Clusters with Solvent-Modulated Europium Luminescence. *Eur. J. Inorg. Chem.* **2012**, *2012*, 3273−3282.

(15) Weiss, C. J.; Marks, T. J. Organo-f-element catalysts for efficient and highly selective hydroalkoxylation and hydrothiolation. *Dalton Trans.* **2010**, *39*, 6576−6588.

(16) Chen, X.-Y.; Yang, X.; Holliday, B. J. Metal-Controlled Assembly of Near-Infrared-Emitting Pentanuclear Lanthanide β-Diketone Clusters. *Inorg. Chem.* **2010**, *49*, 2583−2585.

(17) Petit, S.; Baril-Robert, F.; Pilet, G.; Reber, C.; Luneau, D. Luminescence spectroscopy of europium(III) and terbium(III) penta-, octa- and nonanuclear clusters with β-diketonate ligands. *Dalton Trans.* **2009**, 6809−6815.

(18) Li, X.-L.; W, J.; Tang, J.; Le Guennic, B.; Shi, W.; Cheng, P. A planar triangular Dy^{3+} Dy_3 single-molecule magnet with a toroidal magnetic moment. *Chem. Commun.* **2016**, *52*, 9570−9573.

(19) Wang, H.-L.; Ma, X.-F.; Peng, J.-M.; Zhu, Z.-H.; Li, B.; Zou, H.-H.; Liang, F.-P. Tracking the stepwise formation of the dysprosium cluster (Dy_{10}) with multiple relaxation behavior. *Inorg. Chem.* **2019**, *58*, 9169−9174.

(20) Ma, X.-F.; Wang, H.-L.; Zhu, Z.-H.; Li, B.; Mo, K.-Q.; Zou, H.-H.; Liang, F.-P. Formation of nanocluster $\{Dy_{12}\}$ containing Dy-exclusive vertex-sharing $[Dy_4(\mu^3\text{-}OH)_4]$ cubanes via simultaneous multitemplate guided and step-by-step assembly. *Dalton Trans.* **2019**, *48*, 11338−11344.

(21) Richardson, P.; Hsu, T.-J.; Kuo, C.-J.; Holmberg, R. J.; Gabidullin, B.; Rouzières, M.; Clérac, R.; Murugesu, M.; Lin, P.-H. $[Ln_{16}]$ complexes (Ln= Gd^{III}, Dy^{III}): molecular analogues of natural minerals such as hydrotalcite. *Dalton Trans.* **2018**, *47*, 12847−12851.

(22) D'Alessio, D.; Sobolev, A. N.; Skelton, B. W.; Fuller, R. O.; Woodward, R. C.; Lengkeek, N. A.; Fraser, B. H.; Massi, M.; Ogden, M. I. Lanthanoid "Bottlebrush" Clusters: Remarkably Elongated Metal−Oxo Core Structures with Controllable Lengths. *J. Am. Chem. Soc.* **2014**, *136*, 15122−15125.

(23) Wu, M.; Jiang, F.; Kong, X.; Yuan, D.; Long, L.; Al-Thabaiti, S. A.; Hong, M. Two polymeric 36-metal pure lanthanide nanosize clusters. *Chem. Sci.* **2013**, *4*, 3104−3109.

(24) Chen, L.; Guo, J.-Y.; Xu, X.; Ju, W.-W.; Zhang, D.; Zhu, D.-R.; Xu, Y. A novel 2-D coordination polymer constructed from high-nuclearity waist drum-like pure Ho_{48} clusters. *Chem. Commun.* **2013**, *49*, 9728−9730.

(25) Wu, M.; Jiang, F.; Yuan, D.; Pang, J.; Qian, J.; Al-Thabaiti, S. A.; Hong, M. Polymeric double-anion templated Er_{48} nanotubes. *Chem. Commun.* **2014**, *50*, 1113−1115.

(26) Peng, J.-B.; Kong, X.-J.; Zhang, Q.-C.; Orendáč, M.; Prokleška, J.; Ren, Y.-P.; Long, L.-S.; Zheng, Z.; Zheng, L.-S. Beauty, Symmetry, and Magnetocaloric Effect—Four-Shell Keplerates with 104 Lanthanide Atoms. *J. Am. Chem. Soc.* **2014**, *136*, 17938−17941.

(27) Kuriki, K.; Koike, Y.; Okamoto, Y. Plastic Optical Fiber Lasers and Amplifiers Containing Lanthanide Complexes. *Chem. Rev.* **2002**, *102*, 2347−2356.

(28) Eliseeva, S. V.; Bünzli, J.-C. G. Lanthanide luminescence for functional materials and bio-sciences. *Chem. Soc. Rev.* **2010**, *39*, 189−227.

(29) Omagari, S.; Nakanishi, T.; Seki, T.; Kitagawa, Y.; Takahata, Y.; Fushimi, K.; Ito, H.; Hasegawa, Y. Effective photosensitized energy transfer of nonanuclear terbium clusters using methyl salicylate derivatives. *J. Phys. Chem. A* **2015**, *119*, 1943−1947.

(30) Chen, X. Y.; Yang, X.; Holliday, B. J. Metal-controlled assembly of near-infrared-emitting pentanuclear lanthanide beta-diketone clusters. *Inorg. Chem.* **2010**, *49*, 2583−2585.

(31) Mooibroek, T. J.; Gamez, P.; Pevec, A.; Kasunic, M.; Kozlevcar, B.; Fu, W. T.; Reedijk, J. Efficient, stable, tunable, and easy to synthesize, handle and recycle luminescent materials: $[H_2NMe_2]_3[Ln(III)(2,6\text{-dipicolinolate})_3]$ (Ln = Eu, Tb, or its solid solutions). *Dalton Trans.* **2010**, *39*, 6483−6487.

(32) Knighton, R. C.; Soro, L. K.; Lecointre, A.; Pilet, G.; Fateeva, A.; Pontille, L.; Frances-Soriano, L.; Hildebrandt, N.; Charbonniere, L. J. Upconversion in molecular hetero-nonanuclear lanthanide complexes in solution. *Chem. Commun.* **2021**, *57*, 53−56.

(33) Banerjee, S.; Kumar, G. A.; Riman, R. E.; Emge, T. J.; Brennan, J. G. Oxoclusters of the Lanthanides Begin to Resemble Solid-State Materials at Very Small Cluster Sizes: Structure and NIR Emission from Nd(III). *J. Am. Chem. Soc.* **2007**, *129*, 5926−5931.

(34) Mara, D.; Artizzu, F.; Goura, J.; Jayendran, M.; Bokić, B.; Kolaric, B.; Verbiest, T.; Van Deun, R. Molecular dysprosium complexes for white-light and near-infrared emission controlled by the coordination environment. *J. Lumin.* **2022**, *243*, No. 118646, DOI: 10.1016/j.jlumin.2021.118646.

(35) Aromí, G.; Aguila, D.; Gamez, P.; Luis, F.; Roubeau, O. Design of magnetic coordination complexes for quantum computing. *Chem. Soc. Rev.* **2012**, *41*, 537−546.
(36) Aguilà, D.; Barrios, L. A.; Velasco, V.; Roubeau, O.; Repollés, A.; Alonso, P. J.; Sesé, J.; Teat, S. J.; Luis, F.; Aromí, G. Heterodimetallic [LnLn′] Lanthanide Complexes: Toward a Chemical Design of Two-Qubit Molecular Spin Quantum Gates. *J. Am. Chem. Soc.* **2014**, *136*, 14215−14222.
(37) Aguilà, D.; Velasco, V.; Barrios, L. A.; González-Fabra, J.; Bo, C.; Teat, S. J.; Roubeau, O.; Aromí, G. Selective Lanthanide Distribution within a Comprehensive Series of Heterometallic [LnPr] Complexes. *Inorg. Chem.* **2018**, *57*, 8429−8439.
(38) Liu, J.-L.; Chen, Y.-C.; Guo, F.-S.; Tong, M.-L. Recent advances in the design of magnetic molecules for use as cryogenic magnetic coolants. *Coord. Chem. Rev.* **2014**, *281*, 26−49.
(39) Konieczny, P.; Sas, W.; Czernia, D.; Pacanowska, A.; Fitta, M.; Pelka, R. Magnetic cooling: a molecular perspective. *Dalton Trans.* **2022**, *51*, 12762−12780.
(40) Chen, Y.-C.; Qin, L.; Meng, Z.-S.; Yang, D.-F.; Wu, C.; Fu, Z.; Zheng, Y.-Z.; Liu, J.-L.; Tarasenko, R.; Orendáč, M.; Prokleška, J.; Sechovský, V.; Tong, M.-L. Study of a magnetic-cooling material $Gd(OH)CO_3$. *J. Mater. Chem. A* **2014**, *2*, 9851−9858.
(41) Qiu, J.-Z.; Chen, Y.-C.; Wang, L.-F.; Li, Q.-w.; Orendáč, M.; Tong, M.-L. The effect of magnetic coupling on magneto-caloric behaviour in two 3D Gd(III)−glycolate coordination polymers. *Inorg. Chem. Front.* **2016**, *3*, 150−156.
(42) Cui, C.; Ju, W.; Luo, X.; Lin, Q.; Cao, J.; Xu, Y. A Series of Lanthanide Compounds Constructed from Ln_8 Rings Exhibiting Large Magnetocaloric Effect and Interesting Luminescence. *Inorg. Chem.* **2018**, *57*, 8608−8614.
(43) Lu, J.; Montigaud, V.; Cador, O.; Wu, J.; Zhao, L.; Li, X. L.; Guo, M.; Le Guennic, B.; Tang, J. Lanthanide(III) Hexanuclear Circular Helicates: Slow Magnetic Relaxation, Toroidal Arrangement of Magnetic Moments, and Magnetocaloric Effects. *Inorg. Chem.* **2019**, *58*, 11903−11911.
(44) Hu, P.; Li, S.; Cao, L.; Liu, A.; Zhuang, G. L.; Ji, L.; Li, B. Construction of a High Nuclear Gadolinium Cluster with Enhanced Magnetocaloric Effect through Structural Transition. *ACS Omega* **2022**, *7*, 38782−38788.
(45) Gao, H.-L.; Wang, N.-N.; Wang, W.-M.; Shen, H.-Y.; Zhou, X.-P.; Chang, Y.-X.; Zhang, R.-X.; Cui, J.-Z. Fine-tuning the magnetocaloric effect and SMMs behaviors of coplanar RE_4 complexes by β-diketonate coligands. *Inorg. Chem. Front.* **2017**, *4*, 860−870.
(46) Yao, M.-X.; Cai, L.-Z.; Deng, X.-W.; Zhang, W.; Liu, S.-J.; Cai, X.-M. Self-assembly of rare octanuclear quad (double-stranded) cluster helicates showing slow magnetic relaxation and the magnetocaloric effect. *New J. Chem.* **2018**, *42*, 17652−17658.
(47) Guan, X.-F.; Hou, W.-Y.; Qiao, X.-Y.; Zhang, Z.-Q.; Liu, K.-X.; Wang, W.-M.; Shi, Y.; Pan, F. Synthesis, structures and magnetic refrigeration of two rhombus-shaped Gd_4 cages. *Inorg. Chim. Acta* **2019**, *484*, 47−51.
(48) Marin, R.; Halimi, I.; Errulat, D.; Mazouzi, Y.; Lucchini, G.; Speghini, A.; Murugesu, M.; Hemmer, E. Harnessing the Synergy between Upconverting Nanoparticles and Lanthanide Complexes in a Multiwavelength-Responsive Hybrid System. *ACS Photonics* **2019**, *6*, 436−445.
(49) Wang, W.-M.; Gao, Y.; Yue, R.-X.; Qiao, N.; Wang, D.-T.; Shi, Y.; Zhang, H.; Cui, J.-Z. Construction of a family of Ln_3 clusters using multidentate Schiff base and β-diketonate ligands: fluorescence properties, magnetocaloric effect and slow magnetic relaxation. *New J. Chem.* **2020**, *44*, 9230−9237.
(50) Alexandropoulos, D. I.; Mukherjee, S.; Papatriantafyllopoulou, C.; Raptopoulou, C. P.; Psycharis, V.; Bekiari, V.; Christou, G.; Stamatatos, T. C. A new family of nonanuclear lanthanide clusters displaying magnetic and optical properties. *Inorg. Chem.* **2011**, *50*, 11276−11278.
(51) Mylonas-Margaritis, I.; Kitos, A. A.; Panteli, C. C.; Skordi, K.; Tasiopoulos, A. J.; Bekiari, V.; Escuer, A.; Perlepes, S. P. 2-hydroxybenzophenone-controlled self-assembly of enneanuclear lanthanide(III) hydroxo coordination clusters with an "hourglass"-like topology. *Inorg. Chem. Commun.* **2017**, *83*, 118−122.
(52) Zheng, X.-Y.; Peng, J.-B.; Livera, M. M. V. S.; Luo, Y.; Wang, Y.-Y.; Kong, X.-J.; Long, L.-S.; Zheng, Z.; Zheng, L.-S. Selective Formation of Chromogen I from N-Acetyl-d-glucosamine upon Lanthanide Coordination. *Inorg. Chem.* **2017**, *56*, 110−113.
(53) Chen, H.; Yang, X.; Jiang, D.; Shi, D.; Zhang, L. Construction of NIR luminescent polynuclear lanthanide-based nanoclusters with sensing properties towards metal ions. *Dalton Trans.* **2018**, *47*, 13880−13886.
(54) Wang, H.-S.; Long, Q.-Q.; Yin, C.-L.; Xu, Z.-W.; Pan, Z.-Q. Syntheses, crystal structures and magnetic properties of sandglass Dy_9^{III} and irregular tetrahedron Dy_4^{III} complexes. *Polyhedron* **2018**, *141*, 69−76.
(55) Huang, Y.; Qin, Y.; Ge, Y.; Cui, Y.; Zhang, X.; Li, Y.; Yao, J. Rationally assembled nonanuclear lanthanide clusters: Dy_9 displays slow relaxation of magnetization and Tb_9 serves as luminescent sensor for Fe^{3+}, CrO_4^{2-} and $Cr_2O_7^{2-}$. *New J. Chem.* **2019**, *43*, 19344−19354.
(56) Hu, P.; Cao, L. H.; Liu, A. G.; Zhang, Y. Q.; Zhang, T. L.; Li, B. Modulating the relaxation dynamics via structural transition from a dinuclear dysprosium cluster to a nonanuclear cluster. *Dalton Trans.* **2021**, *50*, 12814−12820.
(57) Li, Z.; Wang, D.; Zhou, Z.; Zhao, G.; Li, Q.; Bi, Y.; Zheng, Z. Thiacalix[4]arene-Sandwiched Sandglass-like Ln_9 Clusters (Ln = Tb and Eu): Insights into the Selective Luminescence Quenching Properties by p-Nitrobenzene Derivatives. *Inorg. Chem.* **2022**, *61*, 20814−20823.
(58) Xu, G.; Wang, Z. M.; He, Z.; Lü, Z.; Liao, C. S.; Yan, C. H. Synthesis and Structural Characterization of Nonanuclear Lanthanide Complexes. *Inorg. Chem.* **2002**, *41*, 6802−6807.
(59) Llunell, M.; Casanova, D.; Cirera, J.; Bofill, J.; Alemany, P.; Alvarez, S. *SHAPE*, version 2.1; Barcelona, 2010.
(60) SeethaLekshmi, S.; Ramya, A. R.; Reddy, M. L. P.; Varughese, S. Lanthanide complex-derived white-light emitting solids: A survey on design strategies. *J. Photochem. Photobiol., C* **2017**, *33*, 109−131.
(61) Mazarakioti, E. C.; Poole, K. M.; Cunha-Silva, L.; Christou, G.; Stamatatos, T. C. A new family of Ln_7 clusters with an ideal D_{3h} metal-centered trigonal prismatic geometry, and SMM and photoluminescence behaviors. *Dalton Trans.* **2014**, *43*, 11456−11460.
(62) Feng, J.; Zhou, L.; Song, S.-Y.; Li, Z.-F.; Fan, W.-Q.; Sun, L.-N.; Yu, Y.-N.; Zhang, H.-J. A study on the near-infrared luminescent properties of xerogel materials doped with dysprosium complexes. *Dalton Trans.* **2009**, 6593−6598, DOI: 10.1039/B906419B.
(63) Dexter, D. L. A theory of sensitized luminescence in solids. *J. Chem. Phys.* **1953**, *21*, 836−850.
(64) Hong, Y.; Lam, J. W. Y.; Tang, B. Z. Aggregation-induced emission: phenomenon, mechanism and applications. *Chem. Commun.* **2009**, 4332−4353.
(65) Hu, R.; Lager, E.; Aguilar-Aguilar, A.; Liu, J.; Lam, J. W. Y.; Sung, H. H. Y.; Williams, I. D.; Zhong, Y.; Wong, K. S.; Peña-Cabrera, E.; Tang, B. Z. Twisted Intramolecular Charge Transfer and Aggregation-Induced Emission of BODIPY Derivatives. *J. Phys. Chem. C* **2009**, *113*, 15845−15853.
(66) Marin, R.; Brunet, G.; Murugesu, M. Shining New Light on Multifunctional Lanthanide Single-Molecule Magnets. *Angew. Chem., Int. Ed.* **2021**, *60*, 1728−1746.
(67) Wang, Q.; Yu, Y.-T.; Wang, J.-L.; Li, J.-N.; Li, N.-F.; Fan, X.; Xu, Y. Two Windmill-Shaped Ln_{18} Nanoclusters Exhibiting High Magnetocaloric Effect and Luminescence. *Inorg. Chem.* **2023**, *62*, 3162−3169.
(68) Wang, W. M.; Xin, X. Y.; Qiao, N.; Wu, Z. L.; Li, L.; Zou, J. Y. Self-assembly of octanuclear Ln(III)-based clusters: their large magnetocaloric effects and highly efficient conversion of CO_2. *Dalton Trans.* **2022**, *51*, 13957−13969.
(69) Noodleman, L. Valence bond description of antiferromagnetic coupling in transition metal dimers. *J. Chem. Phys.* **1981**, *74*, 5737−5743.
(70) Lines, M. E. Orbital angular momentum in the theory of paramagnetic clusters. *J. Chem. Phys.* **1971**, *55*, 2977−2984.

https://doi.org/10.1021/acs.inorgchem.4c00332
Inorg. Chem. 2024, 63, 11963−11976

(71) Chibotaru, L.; Ungur, L. *The Computer Programs SINGLE_ANISO and POLY_ANISO*; University of Leuven, 2006.
(72) Rajeshkumar, T.; Singh, S. K.; Rajaraman, G. A computational perspective on magnetic coupling, magneto-structural correlations and magneto-caloric effect of a ferromagnetically coupled {Gd^{III}−Gd^{III}} Pair. *Polyhedron* **2013**, *52*, 1299−1305.
(73) Singh, M. K.; Rajeshkumar, T.; Kumar, R.; Singh, S. K.; Rajaraman, G. Role of (1, 3){Cu-Cu} Interaction on the Magneto-Caloric Effect of Trinuclear {Cu^{II}-Gd^{III}-Cu^{II}} Complexes: Combined DFT and Experimental Studies. *Inorg. Chem.* **2018**, *57*, 1846−1858.
(74) Chauhan, D.; Vignesh, K. R.; Swain, A.; Langley, S. K.; Murray, K. S.; Shanmugam, M.; Rajaraman, G. Exploiting Strong {Cr^{III}−Dy^{III}} Ferromagnetic Exchange Coupling to Quench Quantum Tunneling of Magnetization in a Novel {$Cr_2^{III}Dy_3^{III}$} Single-Molecule Magnet. *Cryst. Growth Des.* **2023**, *23*, 197−206.
(75) Li, X.-L.; Tang, J. Recent developments in single-molecule toroics. *Dalton Trans.* **2019**, *48*, 15358−15370.
(76) Guo, P.-H.; Liu, J.-L.; Zhang, Z.-M.; Ungur, L.; Chibotaru, L. F.; Leng, J.-D.; Guo, F.-S.; Tong, M.-L. The first {Dy_4} single-molecule magnet with a toroidal magnetic moment in the ground state. *Inorg. Chem.* **2012**, *51*, 1233−1235.
(77) Sørensen, M. A.; Hansen, U. B.; Perfetti, M.; Pedersen, K. S.; Bartolomé, E.; Simeoni, G. G.; Mutka, H.; Rols, S.; Jeong, M.; Zivkovic, I.; et al. Chemical tunnel-splitting-engineering in a dysprosium-based molecular nanomagnet. *Nat. Commun.* **2018**, *9*, No. 1292, DOI: 10.1038/s41467-018-03706-x.
(78) Vincent, R.; Klyatskaya, S.; Ruben, M.; Wernsdorfer, W.; Balestro, F. Electronic read-out of a single nuclear spin using a molecular spin transistor. *Nature* **2012**, *488*, 357−360.
(79) Valeur, B.; Berberan-Santos, M. N. *Molecular Fluorescence: Principles and Applications*; John Wiley & Sons, 2012.
(80) Jiang, S.-D.; Wang, B.-W.; Su, G.; Wang, Z.-M.; Gao, S. A Mononuclear Dysprosium Complex Featuring Single-Molecule-Magnet Behavior. *Angew. Chem., Int. Ed.* **2010**, *49*, 7448−7451.
(81) Anonymous. *CrysAlis PRO*; Rigaku Oxford Diffraction Ltd: Yarnton, England, 2017.
(82) Dolomanov, O. V.; Bourhis, L. J.; Gildea, R. J.; Howard, J. A. K.; Puschmann, H. OLEX2: a complete structure solution, refinement and analysis program. *J. Appl. Crystallogr.* **2009**, *42*, 339−341.
(83) Sheldrick, G. M. SHELXT− Integrated Space-Group and Crystal-Structure Determination. *Acta Crystallogr., Sect. A: Found. Adv.* **2015**, *71*, 3−8.
(84) Sheldrick, G. M. Crystal structure refinement with SHELXL. *Acta Crystallogr., Sect. C: Struct. Chem.* **2015**, *71*, 3−8.
(85) Brandenburg, K. *DIAMOND. Crystal Impact (version 3.1 f) GbR*; Bonn, Germany, 2008.
(86) Bill, E. *julX_2s, Simulation of Molecular Magnetic Data Software*; Max-Planck Institute for Bioinorganic Chemistry: Mülheim, Ruhr, 2014.
(87) Aquilante, F.; Autschbach, J.; Carlson, R. K.; Chibotaru, L. F.; Delcey, M. G.; De Vico, L.; Fdez. Galván, I.; Ferré, N.; Frutos, L. M.; Gagliardi, L. *Molcas 8: New Capabilities for Multiconfigurational Quantum Chemical Calculations across the Periodic Table*; Wiley Online Library, 2016.
(88) Heß, B. A.; Marian, C. M.; Wahlgren, U.; Gropen, O. A mean-field spin-orbit method applicable to correlated wavefunctions. *Chem. Phys. Lett.* **1996**, *251*, 365−371.
(89) Roos, B. O.; Malmqvist, P.-Å. Relativistic quantum chemistry: the multiconfigurational approach. *Phys. Chem. Chem. Phys.* **2004**, *6*, 2919−2927.
(90) Cundari, T. R.; Stevens, W. J. Effective core potential methods for the lanthanides. *J. Chem. Phys.* **1993**, *98*, 5555−5565.

https://doi.org/10.1021/acs.inorgchem.4c00332
Inorg. Chem. 2024, 63, 11963−11976